LANGMUIR

pubs.acs.org/Langmuir Article

Colloidal Stability and Concentration Effects on Nanoparticle Heat Delivery for Magnetic Fluid Hyperthermia

Vanessa Pilati,* Guilherme Gomide, Rafael Cabreira Gomes, Gerardo F. Goya, and Jérôme Depeyrot

Cite This: https://dx.doi.org/10.1021/acs.langmuir.0c03052 Read Online

ACCESS | Metrics & More | Article Recommendations | Supporting Information

ABSTRACT: The heat produced by magnetic nanoparticles, when they are submitted to a time-varying magnetic field, has been used in many auspicious biotechnological applications. In the search for better performance in terms of the specific power absorption (SPA) index, researchers have studied the influence of the chemical composition, size and dispersion, shape, and exchange stiffness in morphochemical structures. Monodisperse assemblies of magnetic nanoparticles have been produced using elaborate synthetic procedures, where the product is generally dispersed in organic solvents. However, the colloidal stability of these rough dispersions has not received much attention in these studies, hampering experimental determination of the SPA. To investigate the influence of colloidal stability on the heating response of ferrofluids, we produced bimagnetic core@shell NPs chemically composed of a ZnMn mixed ferrite core covered by a maghemite shell. Aqueous ferrofluids were prepared with these samples using the electric double layer (EDL) as a strategy to maintain colloidal stability. By starting from a proper sample, ultrastable concentrated ferrofluids were achieved by both tuning the ion/counterion ratio and controlling the water content. As the colloidal stability mainly depends on the ion configuration on the surface of the magnetic nanoparticles, different levels of nanoparticle clustering are achieved by changing the ionic force and pH of the medium. Thus, the samples were submitted to two procedures of EDL destabilization, which involved dilution with an alkaline solution and a neutral pH viscous medium. The SPA results of all prepared ferrofluid samples show a reduction of up to half the efficiency of the standard sample when the ferrofluids are in a neutral pH or concentrated regime. Such results are explained in terms of magnetic dipolar interactions. Our results point to the importance of ferrofluid colloidal stability in a more reliable experimental determination of the NP heat generation performance.

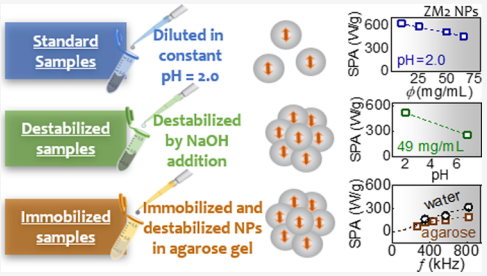

INTRODUCTION

Magnetic nanoparticles (NPs) are a versatile class of multifunctional nanomaterials with numerous applications, such as in environmental remediation,[1−4] agriculture,[5,6] catalysis,[7,8] and biomedicine.[9−14] In the biomedical field, NPs behave like theranostic materials by simultaneously combining different techniques such as diagnosis of diseases and less-invasive local therapies.

The local action of NPs at the cellular level allows therapeutic effects with minimized side effects.[9,15−17] In such a framework, magnetohyperthermia (MHT) mediated by magnetic NPs has arisen as a localized therapeutic strategy shown to be helpful in treating some aggressive types of cancer.[18,19] Phenomenologically, MHT consists of the conversion of electromagnetic energy into heat by irradiating NP assemblies with a radiofrequency magnetic field.[20,21] This local heat delivery can increase the temperature of cancer cell tissues until it induces apoptosis, minimizing the damage to healthy neighboring tissues.[22]

In bulk magnetic materials, several mechanisms contribute to heat generation, such as hysteresis losses, eddy currents, domain wall movements, and resonances of the magnetic moment (μ) with the external field.[23,24] In the case of nanometric materials, some of these processes are negligible because they are energetically disadvantageous, such as magnetic losses associated with eddy currents and magnetic domain wall reorganization. Thus, in such nanomaterials, the main mechanism that contributes to heat generation is the electromagnetic work associated with the forced precession of the magnetic moment induced by the alternating magnetic field[24] H_{AC}.

Several approaches to describe the magnetic losses and therefore predict the magnetic NP energy conversion efficiency have been discussed, such as numerical or analytical solutions of the Landau−Lifshitz−Gilbert equation,[25,26] Stoner−Wohlfarth model-based theories,[27,28] simulations using the Monte Carlo method,[29] and linear response theory (LRT).[21] LRT is the most commonly used model in the literature and has been applied to nanoparticle assemblies[28] with magnetization varying linearly with H in the low magnetic field region. In such cases, the power dissipation density of NPs is given by

Received: October 19, 2020
Revised: December 28, 2020

$$P(\mathrm{W/cm^3}) = \pi\mu_0\chi_0 f {H_0}^2 \frac{2\pi f\tau}{1 + (2\pi f\tau)^2} \quad (1)$$

where μ_0 is the vacuum magnetic permeability, χ_0 is the static initial magnetic susceptibility, f is the frequency of the AC magnetic field, H_0 is the amplitude of the magnetic field, and τ is the effective relaxation time. Originally, Rosensweig suggested that τ was composed of both Néel $\tau_N = \tau_0 \exp(KV/k_BT)$ (τ_0 is the spin magnetic moment reorientation time, which is generally estimated to be 10^{-10} s $< \tau_0 < 10^{-9}$ s, k_B is the Boltzmann constant, and T is the temperature) and Brownian $\tau_B = 3\eta V_h/k_BT$ (η is the medium's viscosity and V_h is the hydrodynamic volume of the NPs) relaxation processes occurring in parallel, allowing us to write $\tau^{-1} = \tau_N^{-1} + \tau_B^{-1}$. More recently, it has been discussed that depending on both the magnetic properties of NPs and the viscosity of the medium in which they are embedded, one of the relaxation processes may be more energetically favorable.[25,30]

The validity of LRT requires at least two conditions to be satisfied: (i) the Zeeman energy must be lower than the thermal energy[21] ($\mu_0\mu H_0/k_BT < 1$) and (ii) the applied magnetic field amplitude must be much smaller than the anisotropy field of the NPs ($H_0 \ll H_a$).[28] In this theory, the power dissipated by NPs, quantified by the specific power absorption (SPA) rate, presents a peak at a frequency that depends on the NP particle size and magnetic anisotropy.[13,21,28]

In the search for better performance materials, certain studies have investigated how some parameters other the NP mean diameter, such as the saturation magnetization,[31−35] morphology,[36−40] magnetic anisotropy,[30,31,40−44] and medium viscosity,[31,33,34,42,45] influence the SPA. However, less attention has been devoted to real cases of NP application, such as effects related to agglomeration and to the collective behavior of the NPs. It is known that the formation of clusters as agglomerates/chains[46] is mainly induced by dipole−dipole interactions. Concerning such effects on MHT, including dispersions in several media,[47−58] reported studies have not shown a clear consensus thus far, with increasing or decreasing SPA observed when the NP concentration (ϕ) is increased. In fact, this collective effect may hinder SPA measurements in power generation studies. Additionally, it represents a real concern related to *in vitro*/*in vivo* applications.

In this context, the aim of this paper is to investigate how the NP concentration and cluster formation may influence the SPA of NP assemblies. We have used ultrastable aqueous ferrofluids (FFs) based on core@shell NPs chemically composed of a core of ZnMn mixed ferrite ($Zn_\delta Mn_{(1-\delta)}Fe_2O_4$—with two different Zn contents, δ = 0.2 and 0.5) covered by a thin maghemite (γ-Fe_2O_3) layer. Such morphochemical composition is recognized for its large SPA[41,59,60] and promising applications in MHT. The electric double layer (EDL) strategy is used to maintain the colloidal stability of the ferrofluids. A density of charges is induced on the NP surface, which consequently creates a double layer of ions, similar to a capacitor model. This cloud of charges screens the electrical potential of the NPs, diminishing the interaction among them. Consequently, entropic repulsion among the NPs appears to prevent aggregation.[61] Therefore, samples with different levels of NP clustering may be achieved by decreasing the ion/counterion ratio in the medium (pH effect). This disturbance of the ionic balance of the solvent medium can induce different states of NP cluster formation and can drive the sample to several colloidal phases (sol, gel, flocculated, and coagulated).[62] Additionally, it is expected that the reduction in the interparticle distance increases the intensity of magnetic dipolar interactions, which consequently may improve cluster formation.

In this paper, we investigate the influence of cluster formation and dipolar interactions on magnetic hyperthermia since these effects are presented in real cases of bioapplications, such as for dispersions of NPs in biological environments.[63,64] We used different approaches to modulate the colloidal stability of our ferrofluids and achieve different levels of cluster formation and dipolar interactions, such as variation of the media pH and NP concentration and NP immobilization in a neutral pH medium. We show, by analyzing MHT assays along with other experimental techniques, that knowledge and control over the parameters that govern colloidal stability are crucial to the understanding of the magnetic processes underlying heat delivery by MHT.

MATERIALS AND METHODS

Synthesis of Nanoparticles and Ferrofluid Preparation. We produced magnetic nanoparticles based on the $Zn_\delta Mn_{(1-\delta)}Fe_2O_4$@$\gamma$-$Fe_2O_3$ composition with two different Zn contents (δ = 0.2 and 0.5). The synthesis of such bimagnetic nanoparticles and their aqueous-based colloidal dispersions follows a three-step procedure:

- The nanoparticles are obtained by a polycondensation reaction of Fe^{3+}, Mn^{2+}, and Zn^{2+} (0.5 M aqueous solutions) in a NaOH medium (2 M) at 100 °C under constant and vigorous stirring. We used Zn/Mn/Fe volume ratios of 0.2:0.8:2 to obtain NPs with a $Zn_{0.2}Mn_{0.8}Fe_2O_4$ chemical composition and 0.5:0.5:2 to obtain NPs with a $Zn_{0.5}Mn_{0.5}Fe_2O_4$ chemical composition, leading to samples named ZM2 and ZM5, respectively. Afterward, the precipitate was magnetically decanted and washed with distilled water.
- The core@shell chemical morphology arises from the surface treatment step, which can be separated into two other steps, acidic washing (HNO_3) to invert the surface charge and hydrothermal treatment with an Fe^{3+} nitrate solution (0.5 M). This procedure creates a thin maghemite surface layer (γ-Fe_2O_3), which protects the ferrite core from acidic dissolution and should modulate the magnetic properties of the NPs.
- Then, the NPs are peptized in the acidic medium (HNO_3) by adjustment of the pH, which establishes the surface charge density, and of the ionic strength, which screens the NP surface potential. This strategy leads to an EDL that prevents NP agglomeration;[61,62] more details about the chemical synthesis of electrostatically stabilized magnetic fluids can be found elsewhere.[41,65,66] Finally, the samples were subjected to successive centrifugation and ultrasonic baths to remove possible NP clusters formed during synthesis.

The NP mean diameter is a key parameter of the power absorption mechanism. It has been reported that increasing the Zn content in the synthesis of ZnMn ferrite NPs induces a reduction in the mean NP diameter.[41,67,68] In the case of the ZM5 sample, we synthesized an auxiliary sample by maintaining all synthesis parameters but slowing down the addition rate of the metallic solution. This strategy was performed to counterbalance the size reduction effect and achieve diameters comparable to those of ZM2 NPs (see results). Therefore, this sample was named ZM5L. In summary, we have produced three ferrofluid samples based on core@shell NPs: ZM2, ZM5, and ZM5L. It is worth emphasizing that our ferrofluids are stabilized in the absence of any additional steric barrier between the NPs.

Sample Preparation. After the synthesis procedure, the ferrofluids are in their crude form, and to enhance the colloidal stability, fine tuning of the pH is necessary. Therefore, samples were submitted to a dialysis procedure, which experimentally consists of putting the crude ferrofluid sample in a dialysis tube with a semipermeable membrane; thereafter, the wrapped sample is left in a HNO_3 (pH = 2.0) aqueous solution bath

https://dx.doi.org/10.1021/acs.langmuir.0c03052
Langmuir XXXX, XXX, XXX−XXX

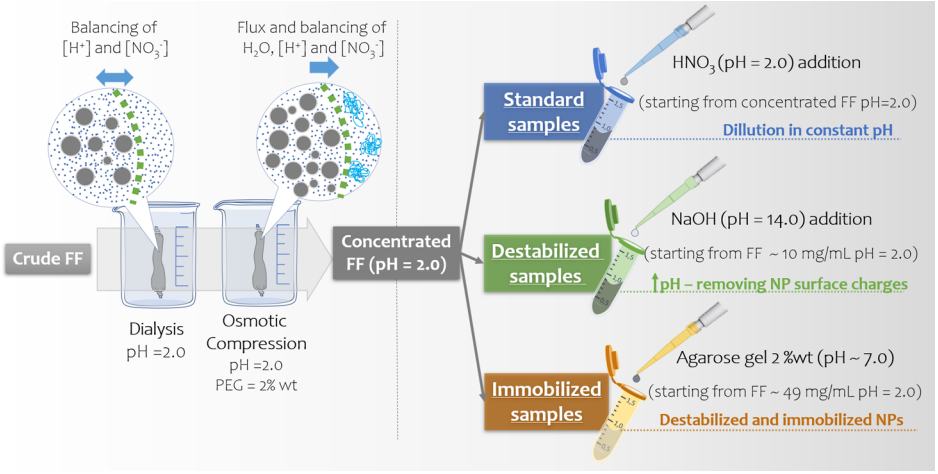

Figure 1. Schematic summary of the sample preparation process. On the left, the first set of procedures, dialysis, and osmotic compression at constant pH is presented. The three classes of prepared samples are presented on the right: standard, destabilized, and immobilized samples.

for some days. This procedure induces a balance of charges inside the ferrofluid sample, consequently improving its colloidal stability.

Then, an osmotic compression procedure[69] was performed to achieve samples in a more concentrated regime. Osmotic compression consists of maintaining the wrapped sample in a bath of a pH-adjusted polyethylene glycol (PEG 35,000) solution (PEG 2% wt; pH = 2.0) for ~15 days, until osmotic pressure stabilizes. We started from diluted ferrofluids with ~10 mg/mL and achieved concentrations of up to 300 mg/mL. The osmotic pressure imposed by the polymer induces a flux of water and charges outward from the semipermeable membrane. It is worth mentioning that the maximum concentrations obtained for each sample are different due to the starting crude ferrofluid volumes. After these procedures, we prepared three kinds of samples, starting from the main concentrated samples.

(i) *Standard samples*—the first set of samples used to measure the heating efficiency through the SPA were obtained by diluting (at constant pH = 2.0) the well-prepared concentrated ferrofluid samples. These samples were considered control samples.

(ii) *Destabilized samples*—to prepare the second set of samples, we took an aliquot of the *standard samples* of ϕ = 49 mg/mL to conduct a destabilization procedure. Experimentally, these *destabilized samples* were obtained by adding a small volume of alkaline solution (NaOH—1 M). Finally, the concentration was then corrected by taking into account the amount of added NaOH solution volume in each case.

(iii) *Immobilized samples*—to study the MHT performance of clusters in a viscous medium, which commonly occurs in biological environments, we dispersed an aliquot of the *standard ferrofluid* in agarose gel. As the polymer preparation requires a pH of ~7 to achieve a high-viscosity gel at room temperature, a deprotonation of the oxonium ions linked to the NP surface is expected, therefore inducing the formation of NP clusters that will be immobilized in the viscous medium. In brief, the fabrication of these samples was conducted as follows. First, the polymer material (viscous gel) was prepared by diluting agarose powder in previously heated (up to ~60 °C) deionized water (2% wt). Afterward, an aliquot of concentrated *standard ferrofluid* was added into the heated gel in the liquid form (~55 °C), and immediate stirring guaranteed proper dispersion of the NPs. Finally, the mixture was let to rest at room temperature in the absence of a magnetic field to become a magnetic gel. The results of prepared samples correspond to ZM2 and ZM5L NPs (due to their similar diameters) at an NP concentration of ~49 mg/mL. A summary of all procedures is presented schematically in Figure 1.

Chemical, Morphological, and Structural Characterization of the NPs. The chemical composition of the NPs was studied *via* the determination of metal concentrations with energy-dispersive X-ray spectroscopy (EDX) and atomic absorption spectroscopy (AAS) techniques. The latter is also applied to determine the concentration of NPs in the studied ferrofluids. Both measurements were conducted at the University of Brasília—UnB—with a Shimadzu EDX 720HS and a Thermo Scientific spectrometer model S series AA, respectively.

The morphology and size distribution of the NPs were checked by transmission electron microscopy (TEM) and high-resolution TEM (HRTEM) using a JEOL JEM-2100. The morphochemical structure of the NPs of the ZM5 sample was investigated by HRTEM using a TECNAI F30 (FEI Co.) installed at Laboratorio de Microscopias Avanzadas (LMA), University of Zaragoza (UZ). Using scanning transmission electron microscopy (STEM) in the high-angle annular dark field (HAADF) mode, we obtained Z-contrast images of the NPs.

The crystalline structure of the NPs was investigated by X-ray diffraction (XRD) after evaporation of the liquid medium of the studied FF. Measurements were conducted at UnB using a D8 Focus (Bruker) diffractometer (Cu Kα radiation with λ = 1.5406 Å) in the range of 10° < 2θ < 90°.

Investigation of Cluster Formation. Dynamic light scattering (DLS) and small-angle X-ray scattering (SAXS) measurements were employed to investigate the size of NPs and the size and morphology of clusters formed in the ferrofluid samples.

DLS measurements were carried out on a 90 Plus particle size analyzer (Brookhaven Instrument Corporation) installed at Instituto de Nanociencia y Materiales de Aragón (INMA). Due to the experimental limitations of the technique, the equipment is only able to measure samples in the diluted regime (ϕ < 2.5 mg/mL). Therefore, measurements were performed in only two situations: for the (i) *standard samples* (ϕ = 2.5 mg/mL; pH = 2.0) obtained in the final dilution procedure and (ii) *destabilized sample* (ϕ = 2.5 mg/mL; pH > 4), achieved at the end of the destabilization process.

The local structure of NPs in the ferrofluid samples was investigated by small-angle X-ray scattering. Measurements were carried out as a function of NP concentration and pH. Experiments were carried out with a Xeuss 2.0 (Xenocs) using a Cu Kα X-ray source and a Dectris Pilatus3R 200K-A bidimensional detector installed at the Physics Institute of University of Brasilia (IF-UnB). During the experiment, samples were conditioned in sealed polyimide tubes with an internal diameter of 700 μm.

The intensity obtained in a SAXS experiment can be understood as the product of the form factor $P(q)$ and the structure factor $S(q)$, as follows

$$I(q) = P(q)S(q) \quad (2)$$

where $q = 4\pi/\lambda$ is the modulus of the scattering vector, $P(q)$ carries information about the shape and size, and $S(q)$ arises from interparticle interactions, being equal to unity for a noninteracting system. This

https://dx.doi.org/10.1021/acs.langmuir.0c03052
Langmuir XXXX, XXX, XXX−XXX

Table 1. Magnetic Nanoparticle and Ferrofluid Characteristics[a]

sample	core composition	$\chi_{M^{2+}}$ before ST	$\chi_{M^{2+}}$ after ST	d_0 (nm)	s	d_X (nm)	$\langle a \rangle$ (nm)	d_h (nm) standard samp.	d_h (nm) destab. samp.
ZM2	$Zn_{0.17}Mn_{0.68}Fe_{1.90}O_4$	0.308(1)	0.241(1)	9.2(1)	0.30(1)	13.9(5)	0.842(1)	48 (pH = 2.0)	650 (pH = 6.8)
ZM5L	$Zn_{0.33}Mn_{0.48}Fe_{2.00}O_4$	0.283(1)	0.227(1)	7.2(1)	0.44(1)	12.4(5)	0.836(1)	50 (pH = 2.0)	420 (pH = 4.0)
ZM5	$Zn_{0.31}Mn_{0.47}Fe_{2.01}O_4$	0.277(1)	0.212(1)	7.4(1)	0.35(1)	10.0(0)	0.840(1)	50 (pH = 2.0)	350 (pH = 4.2)

[a]The columns are the name of the sample, the core chemical composition, the divalent metal fractions of both the core (before surface treatment—ST) and core@shell (after ST), the mean diameter (d_0) and polydispersity index (s) obtained from TEM images, the mean crystalline diameter (d_X) extracted from XRD diffractograms, the mean lattice parameter ($\langle a \rangle$), and the hydrodynamic diameters obtained from DLS measurements for *standard samples* and *destabilized samples* (ϕ < 2.5 mg/mL).

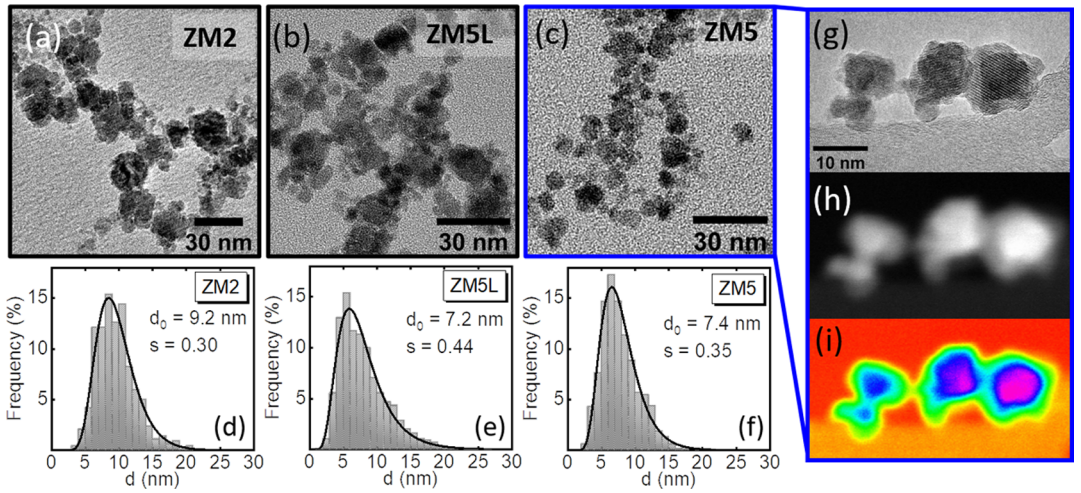

Figure 2. Results from TEM analysis: (a–c) TEM micrographs for ZM2, ZM5L, and ZM5 NPs, respectively. (d–f) Size distribution histograms and the corresponding log-normal fitting for each sample. (g) Representative HRTEM image of ZM5 NPs, (h) Z-contrast HAADF image of the same NPs presented in (g), and (i) artificially colored image modulated by the (g) pixel intensity evidencing the inhomogeneity of the NP chemical composition and the core@shell chemical structure.

simple approach allows us to extract insightful information about the nanosystems in the range from 1 to 100 nm when the samples can be assumed as a noninteracting system. When this is not possible, one must calculate the scattered intensity of the noninteracting system (form factor), which is then compared with the experimental value to obtain information about the structure factor. In this paper, we combine both approaches to extract information about our nanosystems. When calculating the form factor, we model our systems as log-normally distributed spheres.[70] The parameters utilized in the calculations are shown in Table SI1. When obtained using an experimental form factor, the structure factor will be referred to as the effective structure factor $S'(q)$, which will be used here to probe the overall behavior of our ferrofluids. In contrast, the structure factor $S(q)$ will be used to investigate the global balance of interparticle interactions and the presence of clusters in the less-interactive samples.

Magnetic Measurements. Magnetic measurements were carried out in a vibrating sample magnetometer setup (VSM) of a physical property measurement system (PPMS), Quantum Design model 6000, installed in UnB. To perform the basic magnetic characterization of NPs, we used *standard samples* (10 mg/mL) prepared in a plexiglass sample holder. The field dependence of the magnetization, or the hysteresis curve, was obtained at room temperature (300 K) and low temperature (5 K) after a zero field cooling (ZFC) procedure. To ensure magnetic saturation, we used the maximum magnetic field available in the instrument (H_{max} = 7160 kA/m).

Calorimetric Curves. The SPA of all samples was obtained by measuring the temperature when applying AC magnetic fields with frequencies in the range of f = 338–831 kHz and field amplitudes of $4 \leq H_0 \leq 24$ kA/m. These measurements were performed at INMA using a DM100 instrument from nB nanoScale Biomagnetics.

RESULTS AND DISCUSSION

NP Characterization. The chemical composition of the NP core (before the surface treatment) was established from the Zn, Mn, and Fe concentrations obtained from EDX measurements. The results presented in Table 1 show a deficiency of Zn^{2+} ions and Fe^{3+} enrichment in the chemical composition of the nanoparticle core. This feature may be due to the strong alkaline medium (excess OH^- groups) used in the polycondensation reaction, as already reported in the literature.[41,71] After the surface treatment with iron nitrate, the relative amount of Zn^{2+} and Mn^{2+} ions in the NPs decreases because of the local incorporation of Fe^{3+} on the surface. This experimental aspect of sample production has been taken into account using a core@shell chemical model[66] where the iron enrichment is quantified by the molar fraction of divalent metals, given by

$$\chi_{M^{2+}} = \frac{[M^{2+}]}{[M^{2+}] + [Fe^{3+}]} \quad (3)$$

In the case of a stoichiometric ferrite, $\chi_{M^{2+}}$ is equal to 0.33. As we are studying mixed-ferrite cores with variations in the stoichiometric composition covered by a maghemite shell, the obtained results (see Table 1) are in good accordance with the desired morphochemical structure.

Furthermore, in a previous study,[41] the core@shell structure of the ZM5 sample was verified using the STEM technique and quantitatively probed using local EDS. Such an analysis has shown an inhomogeneous maghemite shell (see Figure 2) with an average thickness of approximately 1 nm.[41] Here, we found

https://dx.doi.org/10.1021/acs.langmuir.0c03052
Langmuir XXXX, XXX, XXX–XXX

the same morphochemical structure using Z-contrast HAADF images for the same representative sample (see Figure 2g,h).

The overall analysis of TEM images indicates that the synthesized NPs present a spheroidal rock-shaped morphology (see Figure 2a–c). For all samples, the size distribution histograms are well fitted with a log-normal function (Figure 2d), and the resulting characteristic diameter (d_0) and the standard deviation of the diameter logarithm referred to as the polydispersity index (s) are presented in Table 1.

The crystalline structure of the NPs was checked using XRD measurements. Parameters such as the angular position of diffraction peaks (diffractograms shown in Figure SI1), lattice parameter ($\langle a \rangle$), and interplanar distances are characteristic of the spinel crystalline structure and compare well with the bulk standard data of the International Centre for Diffraction Data (ICDD no. 98-002-8512 to -8516). The crystalline diameter (d_x) of the core@shell NPs is estimated by applying Scherrer's formula to the most intense peak (311), see Table 1 for the results.

Colloidal Stabilization and Clustering of NPs. The prepared FFs have their colloidal stability maintained by an electric potential induced by the deprotonation/protonation equilibrium on the NP/medium interface and is tuned by the ionic strength and pH of the medium. At the end of the dialysis and osmotic compression procedures, the three main samples (*standard samples*) present pH = 2.0 and, consequently, the same ionic strength. The dilution process of samples reduces the NP concentration, while maintaining the physicochemical parameters of the carrier medium constant. Such parameters control the EDL thickness, quantified by the so-called Debye length (κ^{-1}). For instance, an ionic strength of 10^{-2} mol/L yields an ion/counterion thickness of approximately $\kappa^{-1} \sim 3$ nm.

Both *standard samples* and *destabilized* samples were probed by DLS, and the results of *hydrodynamic diameters* (d_h) are presented in Table 1.

In the case of *standard samples* ($\phi = 2.5$ mg/mL), d_h is greater than d_0 and d_x. The results indicate that such samples are dominated by clusters. We should note, however, that such structures, as well as the larger NPs of the size distribution, are more easily detectable with the DLS technique, which may also contribute to the larger d_h values.

For *destabilized samples*, the addition of NaOH into the HNO_3 acidic ferrofluid leads to the formation of water and sodium nitrate ($NaNO_3$). Such a chemical reaction changes the pH of the stable FFs, while sustaining a constant ionic force. The d_h results of this kind of sample show an increase of 8–12× in relation to the values obtained for *standard samples*, evidencing the formation of large clusters. Indeed, this is expected since the addition of the alkaline base promotes the removal of the surface charges that maintained the electrostatic repulsion. Once the point of zero charge is achieved (pH = 7), the FFs coagulate, given the absence of oxonium ions linked to the NP surface.

Figure 3 depicts the collection of SAXS experimental data. As expected, we see, in Figure 3a, that the interactions induced by changes in the NP concentration affect the scattering curves only in the low-q range. We applied the effective structure factor analysis (Figure 3b,e), and the $S'(q)$ curves are typical of similar systems[72−74] and show that we successfully tuned the global balance of interactions from attractive (most dilute samples) to repulsive (concentrations higher than 25 mg/mL).

We carried out form factor calculations, which are shown in Figure 3c for sample ZM2. The structure factor $S(q)$ obtained in this way points to the presence of agglomerates at pH = 2.0 even

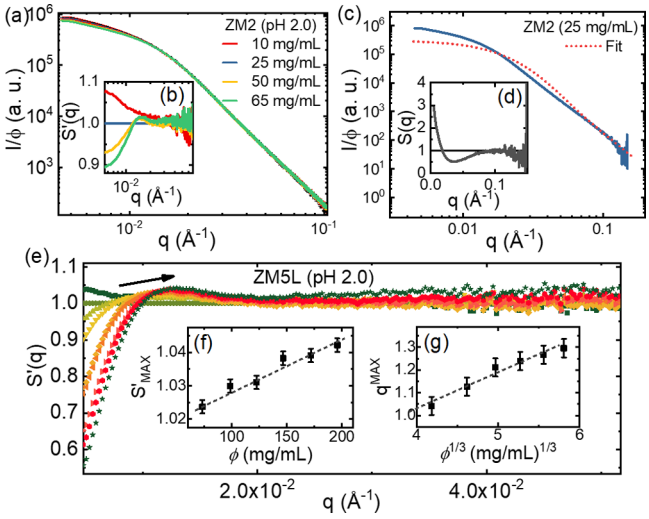

Figure 3. Collection of small-angle X-ray scattering experiments and analysis carried out for the investigated samples. (a) SAXS intensity for sample ZM2 at the optimal pH for different concentrations (pH = 2.0). (b) Effective structure factors obtained considering the sample with 25 mg/mL for the form factor. (c) Scattering curve of the sample considered for the form factor alongside the calculated intensity. The structure factor is then extracted and shown in (d). (e) Experimental structure factors for ZM5L samples at various concentrations. The black arrow indicates increasing concentration. The structure of our fluids is probed by (f) the maximum value of the structure factor as a function of concentration and (g) the q position of the correlation peak plotted against the cubic root of the concentration.

in the less-interactive samples (25 mg/mL). Nevertheless, the evolution of the effective structure factor features with concentration, as seen in Figure 3f,g, indicates a well-structured fluid, even with the presence of such agglomerates.

Magnetic Properties of NPs. In a previous paper, we investigated the magnetic properties at room temperature of a series of samples containing ZM2 and ZM5 in a diluted regime.[41] All magnetization curves of diluted FFs at room temperature presented a giant paramagnetic behavior, with no hysteresis loops as a consequence of both Néel and Brown mechanisms of magnetization relaxation.

Here, we decided to observe the magnetization behavior in low magnetic fields to evaluate the presence of magnetic dipolar interactions. An enlarged view of the field dependence of the magnetization ($\sigma \times H$) at room temperature for *standard samples* (pH = 2.0; ∼10 mg/mL) is presented in Figure 4. Supported by the Langevin formalism, σ_S values are extracted using linear extrapolation in the high-field limit of $\sigma \times 1/H$ curves.[41] The results are presented in Table 2. In the low H region (<12 kA/m), all samples possess a linear dependence on magnetization, see Figure 4a. By considering the low-field limit of the Langevin function, we obtain

$$\frac{\sigma}{H} = \chi_0 \rho_{NP} \tag{4}$$

where χ_0 is the initial susceptibility and ρ_{NP} is the density of NPs, which were previously estimated using the core stoichiometry and crystallographic results[41] (values of ρ_{NP} ranging from 5.06 to 5.25 g/cm^3). Equation 4 was used to fit the data shown in Figure 4, and the χ_0 results are presented in Table 2. Note that the initial magnetic susceptibility of the ZM2 sample is approximately three times those of the other ZM5L and ZM5 samples.

https://dx.doi.org/10.1021/acs.langmuir.0c03052
Langmuir XXXX, XXX, XXX−XXX

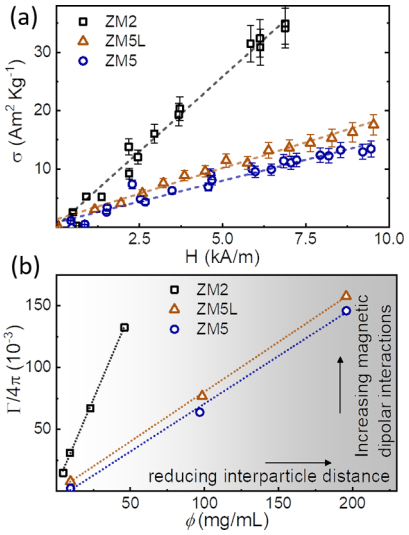

Figure 4. (a) Magnetic field dependence of the magnetization at room temperature in a low-field regime. All magnetic measurements were performed on *standard samples* with low NP concentrations (10 mg/mL). (b) Magnetic coupling parameter ($\Gamma/4\pi$) as a function of NP concentration for *standard samples*.

Table 2. Results Obtained from Magnetic Measurements of *Standard Samples* (pH = 2.0 and $\phi \sim 10$ mg/mL)[a]

sample name	$H_C^{(5K)}$ (KA/m)	$K_{eff}^{(5K)} \times 10^4$ (J/m³)	$K_{eff}^{(300K)\ddagger} \times 10^4$ (J/m³)	$\sigma_S^{(300K)}$ (A m²/kg)	χ_0
ZM2	22(2)*	0.9(1)*	0.2(1)	50(5)*	27(3)
ZM5L	–	–	0.1(1)	–	9.2(9)
ZM5	21(2)	1.1(1)	0.1(1)	40(4)*	7.6(8)

[a]‡: estimated by eq 5, and *: reproduced from Pilati, V.; Cabreira Gomes, R.; Gomide, G.; Coppola, P.; Silva, F. G.; Paula, F. L. O.; Perzynski, R.; Goya, G. F.; Aquino, R.; Depeyrot, J. Core/Shell Nanoparticles of Non-Stoichiometric Zn−Mn and Zn−Co Ferrites as Thermosensitive Heat Sources for Magnetic Fluid Hyperthermia. *The Journal of Physical Chemistry C* **2018**, 122, 3028−3038. Copyright 2020 American Chemical Society.

Furthermore, such measurements also enable the investigation of the magnetic dipolar coupling between NPs by means of the $\Gamma = 3\chi_0\Phi$ expression, with Γ being the dipolar interaction parameter of the FF and Φ being the volumetric fraction of NPs ($\Phi = \phi/\rho_{NP}$). Such magnetic interactions may be considered negligible when $\Gamma/4\pi \ll 1$.[75]

In Figure 4b, we present the $\Gamma/4\pi \times \phi$ curves for the *standard samples*, which show an increase in magnetic interactions when increasing the NP concentration. It is clear that this parameter is determinant in the initial magnetic susceptibility. For instance, samples ZM5 and ZM5L (~100 mg/mL) have comparable interaction parameters greater than that of ZM2 (25 mg/mL), making the global demagnetization effects more relevant in the latter sample.

The results obtained from this approach suggest that magnetic dipolar interactions at room temperature for *standard samples* cannot be considered imperceptible in diluted regimes.

At low temperature (5 K), the zero-field cooled FFs (pH = 2.0; 10 mg/mL) are in a blocked regime, and the $\sigma \times H$ curves present hysteresis. Therefore, by assuming the coercive field H_c of such dilute assemblies to be equal to $0.48H_a$, with H_a being the anisotropy field (randomly oriented single-domain and non-interacting NPs, described by the Stoner−Wohlfarth model[76]), we determined the effective anisotropy constant $K_{eff} = \mu_0 m_s 0.48 H_a$. The results are found in Table 2. However, such values do not present the realistic scenario of MHT due to the difficulty in obtaining K_{eff} values when the samples are in the SPM regime. In addition, recent studies[60,77−79] have shown the importance of considering the thermal dependence of the magnetic anisotropy constant in MHT dynamics and SPA prediction. To estimate K_{eff} values at room temperature, researchers have used the thermal dependencies of the coercive field and saturation magnetization. An estimated value of K can be obtained by the Zener model, written as

$$\frac{K(T)}{K(0)} = \left[\frac{m_s(T)}{m_s(0)}\right]^n \tag{5}$$

where $K(0)$ and $m_s(0)$ are the magnetic anisotropy constant and saturation magnetization at 0 K, respectively, and $m_S(T)$ is Bloch's law given by $m_S(T) = m_S(0)[1 - BT^{1.5}]$, where B is Bloch's constant. The exponent takes the symmetry of the magnetic anisotropy into account, with $n = 3$ for the uniaxial case. The estimated values of the magnetic anisotropy constant at room temperature (K_{eff}(300 K)) are presented in Table 2. Note the decrease by 1 order of magnitude in the magnetic anisotropy constant values compared to those determined at low temperature. These K_{eff}(300 K) are of the magnitude of those of bulk Mn-ferrites.[80]

Magnetic Hyperthermia. The heating efficiency of all prepared samples was quantified by determining the SPA index. Experimentally, it is obtained using the relation

$$\mathrm{SPA(W/g)} = \frac{\rho_S}{\phi} c_S \frac{\Delta T}{\Delta t} \tag{6}$$

where ρ_S and c_S are the density and specific heat of the colloid's solvent medium, respectively, and $\Delta T/\Delta t$ corresponds to the initial rate of the temporal dependence of the temperature increase when H_{AC} is applied to the sample. (See Figure SI2 for a representative curve).

Figure 5a−c shows the SPA × ϕ results of *standard samples*, and Figure 5d−f show the SPA × pH results of *destabilized samples*.

In the case of *standard samples*, it is worth noting that the samples were prepared by performing dialysis and osmotic compression, and afterward, these concentrated samples are standard at constant pH. Measurements at 571 kHz show two distinct behaviors depending on the amplitude of the magnetic field for all samples. In the case of $H_0 = 24$ kA/m, a significant increase in SPA is observed when diluting the sample, a feature that is not observed at a lower magnetic field amplitude. In the case of the ZM2 sample, the concentration range is lower than the others due to the fast heating of the sample during the experiment, which was even faster at higher concentrations, therefore hindering the temperature measurement.

By considering a linear increase in SPA with decreasing ϕ, samples ZM2, ZM5L, and ZM5 possess angular coefficients of 2.85 WL/g², 0.26 WL/g², and 0.023 WL/g², respectively. Such results are in good accordance with those obtained for the dipolar interaction parameter.

The maximum SPA values are obtained at lower ϕ and $H_0 = 24$ kA/m. Nevertheless, the magnitudes for each sample are quite different. The ZM2 sample demonstrates higher efficiency in heat delivery, achieving SPA values of up to 620 W/g (24 kA/m and 571 kHz). This was expected since ZM2 has greater diameter and σ_S, while K_{eff} remains approximately the same.

https://dx.doi.org/10.1021/acs.langmuir.0c03052
Langmuir XXXX, XXX, XXX−XXX

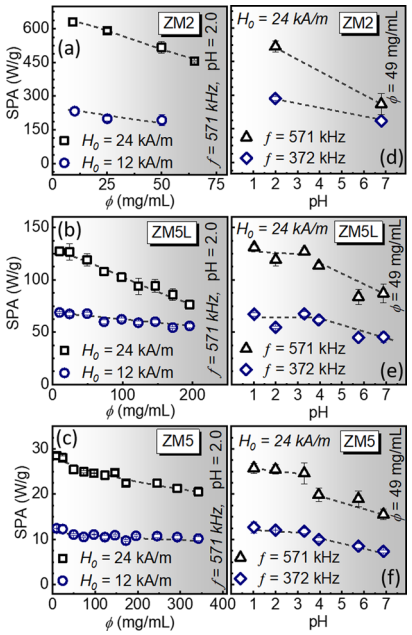

Figure 5. (a–c) Variation in SPA values as a function of concentration for ZM2, ZM5L, and ZM5 FF samples, respectively (with pH = 2.0). (d–f) SPA as a function of pH for ZM2, ZM5L, and ZM5 FF samples, respectively (~49 mg/mL).

When comparing the maximum SPA values of the two similar samples, ZM5 and ZM5L, we identify a difference of approximately five times. Note that the difference between these samples lies in d_x and polydispersity s values, which are higher for the ZM5L sample. This represents an increase in larger NPs in such a sample, which naturally leads to higher SPA values.

Figure 5d–f presents the SPA × pH results for *destabilized samples*. This class of samples has a colloidal stability imbalance when changing the pH of the medium, promoting the formation of NP clusters. Heating curves were obtained in H_0 = 24 kA/m using two frequencies, 372 and 571 kHz. The SPA results show two distinct behaviors for lower and higher pH values. First, at 1 < pH < 4, SPA is approximately constant. Then, at 4 < pH < 7, a decrease in SPA is observed when increasing the pH of the ferrofluids. In the case of measurements at 571 kHz, regardless of the sample, an SPA reduction of ~60% is observed when the pH is ~7.0. In this scenario, the NP surface reaches the maximum deprotonation, leading to the formation of large clusters, and the FFs completely coagulate. A less accentuated behavior is observed for the lower frequency (372 kHz).

Finally, to improve the knowledge about the influence of clusters on the SPA, in Figure 6, we present a qualitative comparison of the evolution of the SPA as a function of H_0 and f of *immobilized* and *standard samples* at similar concentrations (~49 mg/mL). We observe that SPA increases when both H_0 and f increase. However, the *immobilized samples* always demonstrate an SPA lower than that demonstrated by the *standard samples*, regardless of the combination of measuring parameters.

Role of Aggregation and Interparticle Distances. The main goal of this work is to investigate how the interparticle distances (*i.e.*, NP concentration) and cluster formation may influence the SPA. Although the samples studied in this work possess a slight deviation in the core chemical stoichiometry from the nominal composition, they have essentially the same shape, chemical morphology, crystalline phase, and magnetic anisotropy.

We have already studied the MHT performance of these materials in FFs in their crude form and dilute assemblies.[41] Thus, to control ϕ and cluster formation, we performed a set of systematic procedures for ferrofluid preparation, which involved dialysis, osmotic compression, and dilution. Two groups of samples resulted from such procedures. In the main group, named *standard samples*, we investigated the SPA as a function of

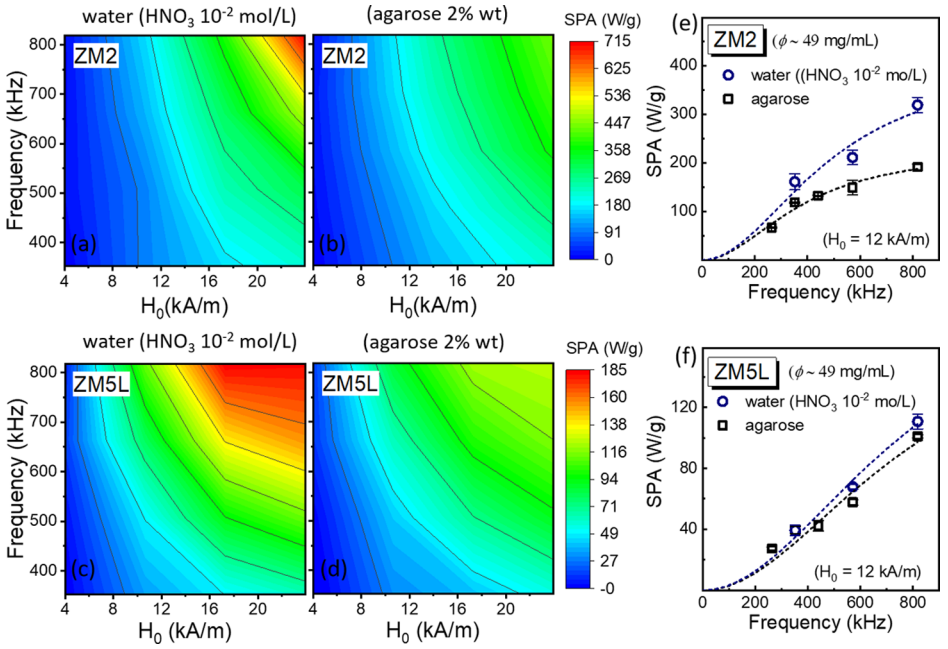

Figure 6. Variations in SPA as a function of f and H_0 for (a) ZM2 and (c) ZM5L NPs dispersed in HNO_3 (10^{-2} mol/L) and (b,d) in agarose gel. Measurements were obtained using a concentration of ~49 mg/mL for both cases. (e) and (f) Frequency dependence of the SPA for NPs from ZM2 and ZM5L samples, both dispersed in water (HNO_3 10^{-2} mol/L) and agarose gel. The fitting corresponds to the LRT approximation.

https://dx.doi.org/10.1021/acs.langmuir.0c03052
Langmuir XXXX, XXX, XXX–XXX

ferrofluid concentration. In the second group, which originated from an aliquot of the *standard samples*, we measured the SPA as a function of pH.

In the *standard samples*, the repulsion among NPs is ensured by entropic forces generated by the EDL, and an increase in the NP concentration in the FFs at constant pH leads to a reduction in the interparticle distance without the formation of larger clusters, as indicated by the SAXS results (Figure 3). The increase in S_{MAX}' with ϕ that we observed in Figure 3f is characteristic of well-structured fluids that do not show evidence of a glassy transition.[73] This fact is also represented by the scaling of q_{MAX} with $\phi^{1/3}$.

Such combined analysis indicates that the fraction of aggregates already present in *standard samples* remains well dispersed as the concentration increases. In fact, the structure factor $S(q)$ in Figure 3d shows a typical attractive behavior, and the extrapolation to $q = 0$ indicates the presence of agglomerates with an average of three to four particles, following the trend of the DLS results for pH 2.0.

In the case of *destabilized samples*, the increased pH induces deprotonation of the NP surface, leading to a reduction in the electrical charges that surround the NPs. Consequently, such a procedure reduces the electrostatic barrier among the NPs, therefore allowing the formation of NP clusters. These features are well observed in DLS measurements, with larger hydrodynamic diameters for larger pH values.

The magnetic characterization of dipolar interactions at room temperature has shown that for an FF in a dilute regime of ∼10 mg/mL, such interactions are present but with very low intensity, especially for ZM5 and ZM5L samples. Indeed, at room temperature, thermal agitation plays an important role in the magnetic behavior of the ensemble of NPs, which naturally leads to a small global effect of dipolar interactions. However, when the concentration increases, the intensity of such interactions also increases, given the reduction in the interparticle distance. In addition, with increasing concentration, the dipolar coupling grows much more for NPs with greater initial susceptibility, such as ZM2 NPs, followed by ZM5L and ZM5 NPs.

Considering the wide size distribution of the studied samples, it is important to note that the low-field magnetization curve, which in fact is a straight line up to ∼12 kA/m for all samples, corresponds to the alignment of the largest NPs of the distribution in the direction of the magnetic field. These particles are those that contribute most to heat generation. On the other hand, the smaller particles require fields with higher intensity to align in the field direction, and therefore, their contribution to the SPA vanishes. Therefore, we must take into account that, for polydisperse systems, only a fraction of NPs in the sample will contribute to the heat generation.

In MHT, data interpretation may be helpful for characterizing the NP magnetic regime (superparamagnetic—SPM—or blocked) at room temperature and in the studied frequency regime. The transition between such magnetic regimes in polydisperse NPs is characterized by a mean blocking temperature $\langle T_B \rangle$, which is given by

$$\langle T_B \rangle = \frac{K_{eff} V}{k_B \ln(t/\tau_0)} \quad (7)$$

where V is the NP mean volume and t is the measurement time ($1.2 \times 10^{-6} < t < 3.0 \times 10^{-6}$ s for MHT measurements). It is worth emphasizing that the blocking temperature of real NP systems consists of a distribution of blocking temperatures. Additionally, its value depends on the frequency regime we are dealing with. For a specific temperature, eq 7 may be translated into a mean blocking volume $\langle V_B \rangle$, which divides the system into a group of SPM NPs ($V < \langle V_B \rangle$) and a fraction of blocked NPs ($V > \langle V_B \rangle$). It has been suggested that a larger fraction of blocked NPs leads to a reduction in heat delivery at low magnetic field amplitudes.[78]

Given the thermal dependence of the anisotropy constant K_{eff}, demonstrated by eq 5, and its role in the transition between blocked and SPM magnetic regimes, a reduction in K_{eff} at room temperature (see Table 2) induces an increase in the blocking volume. For $T = 300$ K and f ranging from 338 to 831 kHz, we obtained critical blocking diameters above 32 nm (ZM2) and 35 nm (ZM5), indicating that all of the NPs of these samples are in the SPM regime at room temperature (see the size distribution in Figure 2d–f).

From the heating curves, our results have shown that both increasing aggregation and increasing NP concentration tend to reduce the heating efficiency of our core@shell NPs. Such a tendency seems to be related to an increased dipolar coupling between NPs, most likely related to a reduction in the interparticle distance.

When our NPs are dispersed in agarose gel, we also observe a reduction in the heating efficiency. Nevertheless, it should be noted that the agarose gel has a very high viscosity, which hinders mechanical rotation, making the Brownian relaxation time much longer than the Néel relaxation time. If we consider the reorientation of the magnetic moment as the main mechanism for the heat delivery, given that the fastest relaxation mechanism contributes predominantly, then, in high-viscosity media, Néel relaxation will be dominant. Nonetheless, in the case of soft-magnetic NPs with lower magnetic anisotropy constants and diameters in the range of 8−12 nm, such as our NPs, Néel relaxation is already the most relevant mechanism even when dispersed in water (HNO_3 10^{-2} mol/L). For instance, considering the hydrodynamic diameters of our samples, both dispersed in water with pH = 2.0 (see Table 1), we estimate Brownian relaxation times (using $\eta = 0.89$ m Pa at 25 °C), leading to 3.7×10^{-5} and 4.2×10^{-5} s for ZM2 and ZM5L NPs, respectively. This means that the mechanical rotation of the NPs do not contribute to the heating in the investigated frequencies (338 kHz < f < 831 kHz). Thus, our results suggest that the decrease in the SPA when NPs are dispersed in agarose gel is most likely related to the formation of clusters due to the lack of colloidal stability in the gel preparation. Figure 6 compares the SPA dependence on frequency (for H_0 = 12 kA/m) of ZM2 and ZM5L NPs dispersed in both water and agarose.

In a previous paper, we discussed the validity of LRT for such NPs in a dilute regime of ∼10 mg/mL and found a quadratic dependence of the SPA on H_0 for low field amplitudes $H_0 < 12$ kA/m, making LRT valid as a first approximation.[41] Considering that our samples are soft magnetic materials, with low anisotropy fields (46 and 44 kA/m for ZM2 and ZM5 NPs, respectively, see H_c values in Table 2, where $H_a = H_c/0.48$), such experimental results are in accordance with the condition $H_0/H_a < 1$. Therefore, using the LRT approximation within its limits of applicability, we fitted the SPA dependence on f using the expression $\text{SPA} = a\frac{(2\pi f)^2\tau}{1+(2\pi f\tau)^2}$, where $a = \frac{\mu_0\chi_0 H_0^2}{2\phi_{NPs}}$ in J g^{-1} units.

From fitting of the experimental data, we extracted a and τ parameters, and the results are depicted in Table SI2. We found

https://dx.doi.org/10.1021/acs.langmuir.0c03052
Langmuir XXXX, XXX, XXX−XXX

relaxation times in the range of 2.0×10^{-7} and 4.2×10^{-7} s, varying very little with the samples and the medium. This corroborates that only Néel relaxation is contributing to the heating in our samples. Such values are in the same order of magnitude of the previously reported values for magnetite, maghemite, Co-ferrite, and Zn−Co ferrite NPs.[31,33,41] To go further, we used the extracted τ values to estimate the effective anisotropy constants K_{eff}^{*} by considering only Néel contribution to the relaxation ($\tau = \tau_{\mathrm{N}}$). Results are depicted in Table SI2, and for ZM2 NPs dispersed in water, it is ∼4.5 times higher than that experimentally obtained through the coercive field and Zener model. The higher difference for ZM5L NPs (∼12×) may be due to its higher polydispersity. Such differences may also be related to NP clustering, which occurs even for pH = 2.0. In addition, the extracted a results lead to χ_0 values extremely distinct from those determined by the low-field DC magnetization measurements. Such divergence may be due to the presence of clusters, which occurs even for the FFs with pH = 2.0, as observed in SAXS measurements. In fact, the NPs arranged in clusters present a smaller interparticle distance, with a subsequent increase in the magnetic coupling from dipolar interactions in such structures. Such a contribution is not accounted for in the LRT, and therefore, our results suggest that this approach is no longer appropriate to describe the NP heat generation in dense assemblies. However, for diluted and noninteracting assemblies, LRT has been a useful tool to describe the NP heat delivery.[33,41]

Our results are in accordance with some previously published studies[52,55,56,81] which also reported a decreasing heating performance with increasing dipolar interactions. Indeed, theoretical models predict that increasing magnetic dipolar interaction yields a decrease in the equilibrium magnetization originated in a disorienting effect of local random magnetic fields.[82] In such a case, a decrease in SPA of interacting assemblies is expected, since it depends on the value of equilibrium magnetization. Nonetheless, other studies suggest that the cooperative organization of NPs into structures such as nanoflowers or chains could be a good strategy to achieve higher efficiency in heat generation.[47,57,58,64] Such diverging trends may be due to intrinsic properties of individual NPs and cluster morphology. More experimental and theoretical studies are needed to elucidate this issue, which remains controversial.

CONCLUSIONS

In summary, we performed a systematic experimental study on bimagnetic core@shell NPs without using any steric strategy to avoid aggregation. NP clustering was controlled and induced here by adjusting the electric charges on the NP surface and in the medium. Through different strategies, our results suggest that the magnetic dipolar interaction contributes negatively to the power absorption of the NPs.

We found that the arrangement of magnetic NPs into collective structures such as clusters and chains represents a challenge in SPA measurement, leading to results that may not be representative of the individual NP heat generation performance. Thus, the description of the heat generation from individual nanoparticles must take into account the colloidal state of the ferrofluids. We propose that future MHT studies on NP power generation take this into account and devote more attention to this issue when considering further bioapplications.

ASSOCIATED CONTENT

Supporting Information

The Supporting Information is available free of charge at https://pubs.acs.org/doi/10.1021/acs.langmuir.0c03052.

Crystalline structure and X-ray diffractograms of the studied nanoparticles, SAXS calculations parameters, representative heating curves, and LRT fitting results (PDF)

AUTHOR INFORMATION

Corresponding Author

Vanessa Pilati − *Complex Fluids Group, Instituto de Física, Universidade de Brasília, 70919-970 Brasília, Brazil;* orcid.org/0000-0002-5517-2091; Email: vanessapilati@gmail.com

Authors

Guilherme Gomide − *Complex Fluids Group, Instituto de Física, Universidade de Brasília, 70919-970 Brasília, Brazil*

Rafael Cabreira Gomes − *Departamento de Física, Universidade Federal de Santa Catarina, 88040-900 Florianópolis, Santa Catarina, Brazil*

Gerardo F. Goya − *Instituto de Nanociencia y Materiales de Aragón (INMA), Universidad de Zaragoza, 50018 Zaragoza, Spain;* orcid.org/0000-0003-1558-9279

Jérôme Depeyrot − *Complex Fluids Group, Instituto de Física, Universidade de Brasília, 70919-970 Brasília, Brazil*

Complete contact information is available at: https://pubs.acs.org/10.1021/acs.langmuir.0c03052

Notes

The authors declare no competing financial interest.

ACKNOWLEDGMENTS

We thank Laboratório Multiusuário de Microscopia de Alta Resolução (LabMic), Universidade de Goiânia (UFG) for TEM measurements and Laboratorio de Microscopias Avanzadas, University of Zaragoza for HRTEM-STEM-HAADF measurements. Authors gratefully acknowledge the financial support of the Brazilian agencies CAPES, CNPq (grants 465259/2014-6, 202340/2015-5, 400849/2016-0, 305796/2016-0, and 422740/2018-7), INCT-FCx (grant 2014/50983-3), and FAP-DF (grants 0193.001569/2017, 0193.001376/2016, and 0193.000.919/2016).

REFERENCES

(1) Shen, Y. F.; Tang, J.; Nie, Z. H.; Wang, Y. D.; Ren, Y.; Zuo, L. Preparation and application of magnetic Fe3O4 nanoparticles for wastewater purification. *Sep. Purif. Technol.* **2009**, *68*, 312−319.

(2) Tang, S. C. N.; Lo, I. M. C. Magnetic nanoparticles: Essential factors for sustainable environmental applications. *Water Res.* **2013**, *47*, 2613−2632.

(3) Sivashankar, R.; Sathya, A. B.; Vasantharaj, K.; Sivasubramanian, V. Magnetic composite an environmental super adsorbent for dye sequestration - A review. *Environ. Nanotechnol. Monit. Manage.* **2014**, *1*−*2*, 36−49.

(4) Campos, A. F. C.; de Oliveira, H. A. L.; da Silva, F. N.; da Silva, F. G.; Coppola, P.; Aquino, R.; Mezzi, A.; Depeyrot, J. Core-Shell Bimagnetic Nanoadsorbents for Hexavalent Chromium Removal from Aqueous Solutions. *J. Hazard. Mater.* **2019**, *362*, 82−91.

(5) Li, J.; Chang, P. R.; Huang, J.; Wang, Y.; Yuan, H.; Ren, H. Physiological Effects of Magnetic Iron Oxide Nanoparticles Towards Watermelon. *J. Nanosci. Nanotechnol.* **2013**, *13*, 5561−5567.

(6) Li, J.; Hu, J.; Ma, C.; Wang, Y.; Wu, C.; Huang, J.; Xing, B. Uptake, translocation and physiological effects of magnetic iron oxide (γ-Fe2O3) nanoparticles in corn (Zea mays L.). *Chemosphere* **2016**, *159*, 326−334.
(7) Faungnawakij, K.; Shimoda, N.; Fukunaga, T.; Kikuchi, R.; Eguchi, K. Crystal structure and surface species of CuFe2O4 spinel catalysts in steam reforming of dimethyl ether. *Appl. Catal., B* **2009**, *92*, 341−350.
(8) Beji, Z.; Sun, M.; Smiri, L. S.; Herbst, F.; Mangeney, C.; Ammar, S. Polyol synthesis of non-stoichiometric Mn-Zn ferrite nanocrystals: structural /microstructural characterization and catalytic application. *RSC Adv.* **2015**, *5*, 65010−65022.
(9) Pankhurst, Q. A.; Connolly, J.; Jones, S. K.; Dobson, J. Applications of magnetic nanoparticles in biomedicine. *J. Phys. D: Appl. Phys.* **2003**, *36*, R167−R181.
(10) Stephen, Z. R.; Kievit, F. M.; Zhang, M. Magnetite nanoparticles for medical MR imaging. *Mater. Today* **2011**, *14*, 330−338.
(11) Arruebo, M.; Fernández-Pacheco, R.; Ibarra, M. R.; Santamaría, J. Magnetic nanoparticles for drug delivery. *Nano Today* **2007**, *2*, 22−32.
(12) Mahmoudi, M.; Sant, S.; Wang, B.; Laurent, S.; Sen, T. Superparamagnetic iron oxide nanoparticles (SPIONs): Development, surface modification and applications in chemotherapy. *Adv. Drug Delivery Rev.* **2011**, *63*, 24−46.
(13) Mehdaoui, B.; Meffre, A.; Carrey, J.; Lachaize, S.; Lacroix, L.-M.; Gougeon, M.; Chaudret, B.; Respaud, M. Optimal Size of Nanoparticles for Magnetic Hyperthermia: A Combined Theoretical and Experimental Study. *Adv. Funct. Mater.* **2011**, *21*, 4573−4581.
(14) Lin, M.; Huang, J.; Sha, M. Recent Advances in Nanosized Mn-Zn Ferrite Magnetic Fluid Hyperthermia for Cancer Treatment. *J. Nanosci. Nanotechnol.* **2014**, *14*, 792−802.
(15) Corchero, J. L.; Villaverde, A. Biomedical applications of distally controlled magnetic nanoparticles. *Trends Biotechnol.* **2009**, *27*, 468−476.
(16) Mah, C.; Fraites, T. J.; Zolotukhin, I.; Song, S.; Flotte, T. R.; Dobson, J.; Batich, C.; Byrne, B. J. Improved method of recombinant AAV2 delivery for systemic targeted gene therapy. *Mol. Ther.* **2002**, *6*, 106−112.
(17) Pankhurst, Q. A.; Thanh, N. T. K.; Jones, S. K.; Dobson, J. Progress in applications of magnetic nanoparticles in biomedicine. *J. Phys. D: Appl. Phys.* **2009**, *42*, 224001.
(18) Johannsen, M.; Gneveckow, U.; Eckelt, L.; Feussner, A.; WaldÖFner, N.; Scholz, R.; Deger, S.; Wust, P.; Loening, S. A.; Jordan, A. Clinical hyperthermia of prostate cancer using magnetic nanoparticles: Presentation of a new interstitial technique. *Int. J. Hyperther.* **2005**, *21*, 637−647.
(19) Maier-Hauff, K.; Rothe, R.; Scholz, R.; Gneveckow, U.; Wust, P.; Thiesen, B.; Feussner, A.; von Deimling, A.; Waldoefner, N.; Felix, R.; Jordan, A. Intracranial Thermotherapy using Magnetic Nanoparticles Combined with External Beam Radiotherapy: Results of a Feasibility Study on Patients with Glioblastoma Multiforme. *J. Neuro Oncol.* **2007**, *81*, 53−60.
(20) Gilchrist, R. K.; Medal, R.; Shorey, W. D.; Hanselman, R. C.; Parrott, J. C.; Taylor, C. B. Selective inductive heating of lymph nodes. *Ann. Surg.* **1957**, *146*, 596−606.
(21) Rosensweig, R. E. Heating magnetic fluid with alternating magnetic field. *J. Magn. Magn. Mater.* **2002**, *252*, 370−374.
(22) Calatayud, M. P.; Soler, E.; Torres, T. E.; Campos-Gonzalez, E.; Junquera, C.; Ibarra, M. R.; Goya, G. F. Cell damage produced by magnetic fluid hyperthermia on microglial BV2 cells. *Sci. Rep.* **2017**, *7*, 8627.
(23) Chikazumi, S. *Physics of Ferromagnetism*; Oxford University Press: New York, 2005; p 655.
(24) López-Ortega, A.; Estrader, M.; Salazar-Alvarez, G.; Roca, A. G.; Nogués, J. Applications of exchange coupled bi-magnetic hard/soft and soft/hard magnetic core/shell nanoparticles. *Phys. Rep.* **2015**, *553*, 1−32.
(25) Usov, N. A.; Liubimov, B. Y. Dynamics of magnetic nanoparticle in a viscous liquid: Application to magnetic nanoparticle hyperthermia. *J. Appl. Phys.* **2012**, *112*, 023901.
(26) Carrião, M. S.; Aquino, V. R. R.; Landi, G. T.; Verde, E. L.; Sousa, M. H.; Bakuzis, A. F. Giant-spin nonlinear response theory of magnetic nanoparticle hyperthermia: A field dependence study. *J. Appl. Phys.* **2017**, *121*, 173901.
(27) Lacroix, L.-M.; Malaki, R. B.; Carrey, J.; Lachaize, S.; Respaud, M.; Goya, G. F.; Chaudret, B. Magnetic hyperthermia in single-domain monodisperse FeCo nanoparticles: Evidences for Stoner-Wohlfarth behavior and large losses. *J. Appl. Phys.* **2009**, *105*, 023911.
(28) Carrey, J.; Mehdaoui, B.; Respaud, M. Simple models for dynamic hysteresis loop calculations of magnetic single-domain nanoparticles: Application to magnetic hyperthermia optimization. *J. Appl. Phys.* **2011**, *109*, 083921−083938.
(29) Vasilakaki, M.; Binns, C.; Trohidou, K. N. Susceptibility losses in heating of magnetic core/shell nanoparticles for hyperthermia: A Monte Carlo study of shape and size effects. *Nanoscale* **2015**, *7*, 7753−7762.
(30) Lima, E.; De Biasi, E.; Zysler, R. D.; Vasquez Mansilla, M.; Mojica-Pisciotti, M. L.; Torres, T. E.; Calatayud, M. P.; Marquina, C.; Ricardo Ibarra, M.; Goya, G. F. Relaxation time diagram for identifying heat generation mechanisms in magnetic fluid hyperthermia. *J. Nanoparticle Res.* **2014**, *16*, 2791.
(31) Fortin, J.-P.; Wilhelm, C.; Servais, J.; Ménager, C.; Bacri, J.-C.; Gazeau, F. Size-Sorted Anionic Iron Oxide Nanomagnets as Colloidal Mediators for Magnetic Hyperthermia. *J. Am. Chem. Soc.* **2007**, *129*, 2628−2635.
(32) Goya, G. F.; Lima, E.; Arelaro, A. D.; Torres, T.; Rechenberg, H. R.; Rossi, L.; Marquina, C.; Ibarra, M. R. Magnetic Hyperthermia With Fe$_{3}$O$_{4}$ Nanoparticles: The Influence of Particle Size on Energy Absorption. *IEEE Trans. Magn.* **2008**, *44*, 4444−4447.
(33) De la Presa, P.; Luengo, Y.; Multigner, M.; Costo, R.; Morales, M. P.; Rivero, G.; Hernando, A. Study of Heating Efficiency as a Function of Concentration, Size, and Applied Field in γ-Fe2O3 Nanoparticles. *J. Phys. Chem. C* **2012**, *116*, 25602−25610.
(34) Vallejo-Fernandez, G.; Whear, O.; Roca, A. G.; Hussain, S.; Timmis, J.; Patel, V.; O'Grady, K. Mechanisms of hyperthermia in magnetic nanoparticles. *J. Phys. D: Appl. Phys.* **2013**, *46*, 312001−312007.
(35) Lima, E.; Torres, T. E.; Rossi, L. M.; Rechenberg, H. R.; Berquo, T. S.; Ibarra, A.; Marquina, C.; Ibarra, M. R.; Goya, G. F. Size dependence of the magnetic relaxation and specific power absorption in iron oxide nanoparticles. *J. Nanoparticle Res.* **2013**, *15*, 1654−1665.
(36) Guardia, P.; Di Corato, R.; Lartigue, L.; Wilhelm, C.; Espinosa, A.; Garcia-Hernandez, M.; Gazeau, F.; Manna, L.; Pellegrino, T. Water-Soluble Iron Oxide Nanocubes with High Values of Specific Absorption Rate for Cancer Cell Hyperthermia Treatment. *ACS Nano* **2012**, *6*, 3080−3091.
(37) Noh, S.-h.; Na, W.; Jang, J.-t.; Lee, J.-H.; Lee, E. J.; Moon, S. H.; Lim, Y.; Shin, J.-S.; Cheon, J. Nanoscale Magnetism Control via Surface and Exchange Anisotropy for Optimized Ferrimagnetic Hysteresis. *Nano Lett.* **2012**, *12*, 3716−3721.
(38) Martinez-Boubeta, C.; Simeonidis, K.; Makridis, A.; Angelakeris, M.; Iglesias, O.; Guardia, P.; Cabot, A.; Yedra, L.; Estradé, S.; Peiró, F.; Saghi, Z.; Midgley, P. A.; Conde-Leborán, I.; Serantes, D.; Baldomir, D. Learning from nature to improve the heat generation of iron-oxide nanoparticles for magnetic hyperthermia applications. *Sci. Rep.* **2013**, *3*, 1652.
(39) Das, R.; Alonso, J.; Nemati Porshokouh, Z.; Kalappattil, V.; Torres, D.; Phan, M.-H.; Garaio, E.; García, J. Á.; Sanchez Llamazares, J. L.; Srikanth, H. Tunable High Aspect Ratio Iron Oxide Nanorods for Enhanced Hyperthermia. *J. Phys. Chem. C* **2016**, *120*, 10086−10093.
(40) Nemati, Z.; Alonso, J.; Martinez, L. M.; Khurshid, H.; Garaio, E.; Garcia, J. A.; Phan, M. H.; Srikanth, H. Enhanced Magnetic Hyperthermia in Iron Oxide Nano-Octopods: Size and Anisotropy Effects. *J. Phys. Chem. C* **2016**, *120*, 8370−8379.
(41) Pilati, V.; Cabreira Gomes, R.; Gomide, G.; Coppola, P.; Silva, F. G.; Paula, F. L. O.; Perzynski, R.; Goya, G. F.; Aquino, R.; Depeyrot, J. Core/Shell Nanoparticles of Non-Stoichiometric Zn-Mn and Zn-Co Ferrites as Thermosensitive Heat Sources for Magnetic Fluid Hyperthermia. *J. Phys. Chem. C* **2018**, *122*, 3028−3038.

https://dx.doi.org/10.1021/acs.langmuir.0c03052
Langmuir XXXX, XXX, XXX−XXX

(42) Verde, E. L.; Landi, G. T.; Gomes, J. A.; Sousa, M. H.; Bakuzis, A. F. Magnetic hyperthermia investigation of cobalt ferrite nanoparticles: Comparison between experiment, linear response theory, and dynamic hysteresis simulations. *J. Appl. Phys.* **2012**, *111*, 123902.
(43) Fantechi, E.; Innocenti, C.; Albino, M.; Lottini, E.; Sangregorio, C. Influence of cobalt doping on the hyperthermic efficiency of magnetite nanoparticles. *J. Magn. Magn. Mater.* **2015**, *380*, 365−371.
(44) Mameli, V.; Musinu, A.; Ardu, A.; Ennas, G.; Peddis, D.; Niznansky, D.; Sangregorio, C.; Innocenti, C.; Thanh, N. T. K.; Cannas, C. Studying the effect of Zn-substitution on the magnetic and hyperthermic properties of cobalt ferrite nanoparticles. *Nanoscale* **2016**, *8*, 10124−10137.
(45) Suto, M.; Hirota, Y.; Mamiya, H.; Fujita, A.; Kasuya, R.; Tohji, K.; Jeyadevan, B. Heat dissipation mechanism of magnetite nanoparticles in magnetic fluid hyperthermia. *J. Magn. Magn. Mater.* **2009**, *321*, 1493−1496.
(46) Itri, R.; Depeyrot, J.; Tourinho, F. A.; Sousa, M. H. Nanoparticle chain-like formation in electrical double-layered magnetic fluids evidenced by small-angle x-ray scattering. *Eur. Phys. J. E: Soft Matter Biol. Phys.* **2001**, *4*, 201−208.
(47) Dennis, C. L.; Jackson, A. J.; Borchers, J. A.; Hoopes, P. J.; Strawbridge, R.; Foreman, A. R.; Van Lierop, J.; Grüttner, C.; Ivkov, R. Nearly complete regression of tumors via collective behavior of magnetic nanoparticles in hyperthermia. *Nanotechnology* **2009**, *20*, 395103.
(48) Serantes, D.; Baldomir, D.; Martinez-Boubeta, C.; Simeonidis, K.; Angelakeris, M.; Natividad, E.; Castro, M.; Mediano, A.; Chen, D.-X.; Sanchez, A.; Balcells, L.; Martínez, B. Influence of dipolar interactions on hyperthermia properties of ferromagnetic particles. *J. Appl. Phys.* **2010**, *108*, 073918.
(49) Urtizberea, A.; Natividad, E.; Arizaga, A.; Castro, M.; Mediano, A. Specific Absorption Rates and Magnetic Properties of Ferrofluids with Interaction Effects at Low Concentrations. *J. Phys. Chem. C* **2010**, *114*, 4916−4922.
(50) Lartigue, L.; Hugounenq, P.; Alloyeau, D.; Clarke, S. P.; Lévy, M.; Bacri, J.-C.; Bazzi, R.; Brougham, D. F.; Wilhelm, C.; Gazeau, F. Cooperative Organization in Iron Oxide Multi-Core Nanoparticles Potentiates Their Efficiency as Heating Mediators and MRI Contrast Agents. *ACS Nano* **2012**, *6*, 10935−10949.
(51) Martinez-Boubeta, C.; Simeonidis, K.; Serantes, D.; Conde-Leborán, I.; Kazakis, I.; Stefanou, G.; Peña, L.; Galceran, R.; Balcells, L.; Monty, C.; Baldomir, D.; Mitrakas, M.; Angelakeris, M. Adjustable Hyperthermia Response of Self-Assembled Ferromagnetic Fe-MgO Core-Shell Nanoparticles by Tuning Dipole-Dipole Interactions. *Adv. Funct. Mater.* **2012**, *22*, 3737−3744.
(52) Branquinho, L. C.; Carrião, M. S.; Costa, A. S.; Zufelato, N.; Sousa, M. H.; Miotto, R.; Ivkov, R.; Bakuzis, A. F. Effect of magnetic dipolar interactions on nanoparticle heating efficiency: Implications for cancer hyperthermia. *Sci. Rep.* **2013**, *3*, 2887.
(53) Saville, S. L.; Qi, B.; Baker, J.; Stone, R.; Camley, R. E.; Livesey, K. L.; Ye, L.; Crawford, T. M.; Thompson Mefford, O. The formation of linear aggregates in magnetic hyperthermia: Implications on specific absorption rate and magnetic anisotropy. *J. Colloid Interface Sci.* **2014**, *424*, 141−151.
(54) Sadat, M. E.; Patel, R.; Sookoor, J.; Bud'ko, S. L.; Ewing, R. C.; Zhang, J.; Xu, H.; Wang, Y.; Pauletti, G. M.; Mast, D. B.; Shi, D. Effect of spatial confinement on magnetic hyperthermia via dipolar interactions in Fe3O4 nanoparticles for biomedical applications. *Mater. Sci. Eng., C* **2014**, *42*, 52−63.
(55) Guibert, C.; Dupuis, V.; Peyre, V.; Fresnais, J. Hyperthermia of Magnetic Nanoparticles: Experimental Study of the Role of Aggregation. *J. Phys. Chem. C* **2015**, *119*, 28148−28154.
(56) Coral, D. F.; Mendoza Zélis, P.; Marciello, M.; Morales, M. d. P.; Craievich, A.; Sánchez, F. H.; Fernández van Raap, M. B. Effect of Nanoclustering and Dipolar Interactions in Heat Generation for Magnetic Hyperthermia. *Langmuir* **2016**, *32*, 1201−1213.
(57) Myrovali, E.; Maniotis, N.; Makridis, A.; Terzopoulou, A.; Ntomprougkidis, V.; Simeonidis, K.; Sakellari, D.; Kalogirou, O.; Samaras, T.; Salikhov, R.; Spasova, M.; Farle, M.; Wiedwald, U.; Angelakeris, M. Arrangement at the nanoscale: Effect on magnetic particle hyperthermia. *Sci. Rep.* **2016**, *6*, 37934.
(58) Hemery, G.; Keyes, A. C.; Garaio, E.; Rodrigo, I.; Garcia, J. A.; Plazaola, F.; Garanger, E.; Sandre, O. Tuning Sizes, Morphologies, and Magnetic Properties of Monocore Versus Multicore Iron Oxide Nanoparticles through the Controlled Addition of Water in the Polyol Synthesis. *Inorg. Chem.* **2017**, *56*, 8232−8243.
(59) Lee, J.-H.; Jang, J.-t.; Choi, J.-s.; Moon, S. H.; Noh, S.-h.; Kim, J.-w.; Kim, J.-G.; Kim, I.-S.; Park, K. I.; Cheon, J. Exchange-coupled magnetic nanoparticles for efficient heat induction. *Nat. Nanotechnol.* **2011**, *6*, 418−422.
(60) Zhang, Q.; Castellanos-Rubio, I.; Munshi, R.; Orue, I.; Pelaz, B.; Gries, K. I.; Parak, W. J.; del Pino, P.; Pralle, A. Model Driven Optimization of Magnetic Anisotropy of Exchange-Coupled Core-Shell Ferrite Nanoparticles for Maximal Hysteretic Loss. *Chem. Mater.* **2015**, *27*, 7380−7387.
(61) Israelachvili, J. *Intermolecular and Surface Forces*; Elsevier Inc., 2011; p 676.
(62) Campos, A. F. C.; Marinho, E. P.; Ferreira, M. d. A.; Tourinho, F. A.; Paula, F. L. d. O.; Depeyrot, J. X-DLVO Interactions between nanocolloidal magnetic particles: the quantitative interpretation of the pH-dependent phase diagram of EDL-MF. *Braz. J. Phys.* **2009**, *39*, 230−235.
(63) Di Corato, R.; Espinosa, A.; Lartigue, L.; Tharaud, M.; Chat, S.; Pellegrino, T.; Ménager, C.; Gazeau, F.; Wilhelm, C. Magnetic hyperthermia efficiency in the cellular environment for different nanoparticle designs. *Biomaterials* **2014**, *35*, 6400−6411.
(64) Sanz, B.; Cabreira-Gomes, R.; Torres, T. E.; Valdés, D. P.; Lima, E.; De Biasi, E.; Zysler, R. D.; Ibarra, M. R.; Goya, G. F. Low-Dimensional Assemblies of Magnetic MnFe2O4 Nanoparticles and Direct In Vitro Measurements of Enhanced Heating Driven by Dipolar Interactions: Implications for Magnetic Hyperthermia. *ACS Appl. Nano Mater.* **2020**, *3*, 8719−8731.
(65) Sousa, M. H.; Tourinho, F. A.; Depeyrot, J.; da Silva, G. J.; Lara, M. C. F. L. New Electric Double-Layered Magnetic Fluids Based on Copper, Nickel, and Zinc Ferrite Nanostructures. *J. Phys. Chem. B* **2001**, *105*, 1168−1175.
(66) Gomes, J. d. A.; Sousa, M. H.; Tourinho, F. A.; Aquino, R.; da Silva, G. J.; Depeyrot, J.; Dubois, E.; Perzynski, R. Synthesis of Core−Shell Ferrite Nanoparticles for Ferrofluids: Chemical and Magnetic Analysis. *J. Phys. Chem. C* **2008**, *112*, 6220−6227.
(67) Rath, C.; Anand, S.; Das, R. P.; Sahu, K. K.; Kulkarni, S. D.; Date, S. K.; Mishra, N. C. Dependence on cation distribution of particle size, lattice parameter, and magnetic properties in nanosize Mn-Zn ferrite. *J. Appl. Phys.* **2002**, *91*, 2211−2215.
(68) Arulmurugan, R.; Vaidyanathan, G.; Sendhilnathan, S.; Jeyadevan, B. Mn-Zn ferrite nanoparticles for ferrofluid preparation: Study on thermal-magnetic properties. *J. Magn. Magn. Mater.* **2006**, *298*, 83−94.
(69) Parsegian, V. A.; Fuller, N.; Rand, R. P. Measured work of deformation and repulsion of lecithin bilayers. *Proc. Natl. Acad. Sci. U.S.A.* **1979**, *76*, 2750−2754.
(70) Kline, S. R. Reduction and analysis of SANS and USANS data using IGOR Pro. *J. Appl. Crystallogr.* **2006**, *39*, 895−900.
(71) Rath, C.; Sahu, K. K.; Anand, S.; Date, S. K.; Mishra, N. C.; Das, R. P. Preparation and characterization of nanosize Mn-Zn ferrite. *J. Magn. Magn Mater.* **1999**, *202*, 77−84.
(72) Filomeno, C. L.; Kouyaté, M.; Peyre, V.; Demouchy, G.; Campos, A. F. C.; Perzynski, R.; Tourinho, F. A.; Dubois, E. Tuning the Solid/Liquid Interface in Ionic Colloidal Dispersions: Influence on Their Structure and Thermodiffusive Properties. *J. Phys. Chem. C* **2017**, *121*, 5539−5550.
(73) Mériguet, G.; Wandersman, E.; Dubois, E.; Cebers, A.; Gomes, J. A.; Demouchy, G.; Depeyrot, J.; Robert, A.; Perzynski, R. Magnetic fluids with tunable interparticle interaction: Monitoring the under-field local structure. *Magnetohydrodynamics* **2012**, *48*, 415−425.
(74) Wandersman, E.; Chushkin, Y.; Dubois, E.; Dupuis, V.; Demouchy, G.; Robert, A.; Perzynski, R. Repulsive and attractive ferroglasses: a SAXS and XPCS study. *Braz. J. Phys.* **2009**, *39*, 210−216.

https://dx.doi.org/10.1021/acs.langmuir.0c03052
Langmuir XXXX, XXX, XXX−XXX

(75) Silva, F. G.; Aquino, R.; Tourinho, F. A.; Stepanov, V. I.; Raikher, Y. L.; Perzynski, R.; Depeyrot, J. The role of magnetic interactions in exchange bias properties of MnFe2O4@γ-Fe2O3core/shell nanoparticles. *J. Phys. D: Appl. Phys.* **2013**, *46*, 285003.
(76) Stoner, E. C.; Wohlfarth, E. A mechanism of magnetic hysteresis in heterogeneous alloys. *Philos. Trans. R. Soc., A* **1948**, *240*, 599−642.
(77) Garaio, E.; Sandre, O.; Collantes, J.-M.; Garcia, J. A.; Mornet, S.; Plazaola, F. Specific absorption rate dependence on temperature in magnetic field hyperthermia measured by dynamic hysteresis losses (ac magnetometry). *Nanotechnology* **2014**, *26*, 015704.
(78) Aquino, V. R. R.; Vinícius-Araújo, M.; Shrivastava, N.; Sousa, M. H.; Coaquira, J. A. H.; Bakuzis, A. F. Role of the fraction of blocked nanoparticles on the hyperthermia efficiency of Mn-based ferrites at clinically relevant conditions. *J. Phys. Chem. C* **2019**, *123*, 27725−27734.
(79) Torres, T. E.; Lima, E., Jr; Mayoral, A.; Ibarra, A.; Marquina, C.; Ibarra, M. R.; Goya, G. F. Validity of the Néel-Arrhenius model for highly anisotropic CoxFe3−xO4nanoparticles. *J. Appl. Phys.* **2015**, *118*, 183902.
(80) Rondinone, A. J.; Liu, C.; Zhang, Z. J. Determination of magnetic anisotropy distribution and anisotropy constant of manganese spinel ferrite nanoparticles. *J. Phys. Chem. B* **2001**, *105*, 7967−7971.
(81) Piñeiro-Redondo, Y.; Bañobre-López, M.; Pardiñas-Blanco, I.; Goya, G.; López-Quintela, M. A.; Rivas, J. The influence of colloidal parameters on the specific power absorption of PAA-coated magnetite nanoparticles. *Nanoscale Res. Lett.* **2011**, *6*, 383.
(82) Usov, N. A.; Serebryokava, O. N. Equilibrium properties of assembly of interacting superparamagnetic nanoparticles. *Sci. Rep.* **2020**, *10*, 13677.

https://dx.doi.org/10.1021/acs.langmuir.0c03052
Langmuir XXXX, XXX, XXX−XXX